INTERLAMINAR TOUGHENING MECHANISMS: IN SITU GROWTH AND MODELLING

G. Borstnar[1], M.N. Mavrogordato[1], Q.D. Yang[2], I. Sinclair[1] and S.M. Spearing[1]

[1] Faculty of Engineering and the Environment, University of Southampton, Highfield,
Southampton SO17 1BJ, UK
Email: G.Borstnar@soton.ac.uk, web page: http://www.southampton.ac.uk

[2] Department of Mechanical and Aerospace Engineering, University of Miami, Coral Gables,
FL 33124, USA
Email: qdyang@miami.edu, web page: http://www.miami.edu

Keywords: CFRPs, Particle-Toughening, Interlaminar toughness, Computed Tomography, Augmented Finite Element Method

ABSTRACT

Modelling composite toughness and what mechanisms are responsible for added toughness has been less tackled within the composites community. With the advances of computational resources and the development of arbitrary cracking models, such as the Augmented Finite Element Method (AFEM), more complex microstructures can now be tackled with multiple interacting cracks. It has been established that Mode I crack propagation in particle-toughened interlayers within a CFRP laminate involve a process zone rather than a distinct crack tip. This involves multiple cracks forming ahead of the main crack that then coalesce and leave behind bridging ligaments that provide traction across the crack flanks. Preliminary idealised 2D AFEM models are presented in this work, that highlight the effects of the relative role of neat resin to ply interface cohesive properties, and the fraction of 'idealised de-bonds'/discontinuities, in keeping the crack path within the interlayer. 4-dimensional time-resolved Computed Tomography (CT) experiments complement the abstract models, with the chronology of damage events and resultant crack paths being directly identified in different toughened microstructures. Additionally, quantification of the bridging behaviour elucidated micromechanical differences between the systems, with the number of bridging ligaments and the total bridged area being quantified and compared to macro-scale toughness. This work is intended to improve understanding around interlaminar toughness, and lead to the development and validation of physically representative micro-mechanical models.

1 INTRODUCTION

Carbon Fibre Reinforced Plastics (CFRPs) are increasingly used in primary aerospace structures, however, significant loss in mechanical properties can be caused by low velocity impact events that may occur in service [1]. The dispersion of secondary phase particles within interlaminar regions has been show to effectively reduce the spread of delaminations caused by impacts via toughening of the interlayer [2]–[4]. Micromechanical understanding and quantification of interlaminar failure processes in these complex particle-toughened interlayers is not well established, with corresponding uncertainty in how added toughness arises precisely. In bulk resins, toughening mechanisms such as; crack pinning [5], crack path deflection [5], [6], particle bridging [7], particle/resin de-bonding and subsequent void growth [8], and localised shear yielding [9] have been identified. However, it has been established that an improvement in bulk resin toughness will not translate directly into an equal improvement in interlaminar toughness, which has been attributed to the constraining action of the surrounding plies [4], [10]. Additionally, fibre interfaces also offer an alternate crack path that may result in propagation along or inside the ply, thus avoiding the toughened interlayer [11], [12]. Previous work has shown that particles can draw the crack path away from the fibre interface by de-bonding ahead of the ‘crack tip’, and that the crack path preferentially follows particle-rich regions ahead of the main crack, thus enabling a more tortuous ligament-rich crack path to develop [13]. Other authors have suggested that in similar particle-toughened systems, smaller, uniformly distributed particles will result in a higher fracture toughness [14], but it is not clear why there appears to be an optimum microstructure.

Through the use of Synchrotron Radiation Computed Tomography (SRCT), *in situ* non-destructive identification of micro-mechanisms is possible within the bulk material while avoiding sectioning artifacts associated with conventional materialography. In this work, time-resolved *in situ* tests have been conducted on four different material systems using a wedge-driven approach to simulate Mode I loading conditions, which can be seen as the most critical loading condition for delaminations. This allowed the influence of local microstructural irregularity on the location of damage initiation and crack path evolution to be observed in a chronological manner. Additionally, the effect of particle type and size on the fracture micro-mechanisms was explored qualitatively, with features such as ligament formation and Crack Opening Displacements (CODs) being quantified following digital segmentation. A preliminary 2D model is presented in this work, where the Augmented-Finite Element Method (AFEM) [15] has been used to simulate a particle-toughened interlayer with idealised particle de-bonds represented by ‘strong discontinuities’. The effects of the relative cohesive strengths of the neat resin and ply interface, and the neighbouring ply stiffness, on the crack path were explored parametrically. This was simulated by varying the fraction of discontinuities ahead of the crack tip and identifying when the crack will propagate to the ply interface. The work aims to build towards more realistic microstructures, whereby the competition between neat resin, particle and ply interface properties can be explored and compared with *in situ* crack growth data.

2 EXPERIMENTAL METHODS

2.1 Materials

Developmental CFRPs were prepared by Cytec Engineered Materials and manufactured and cured according to a standard aerospace autoclave cycle. A 16 ply uni-directional layup (~3 mm thick) was prepared from pre-preg with a 40 μm thick Polytetraflouroethylene (PTFE) insert placed at mid-plane. Proprietary intermediate modulus carbon fibres (~5.4 μm in diameter) were used as the primary reinforcement, and secondary-phase thermoplastic toughening particles were confined to ~30 μm thick interlayers. Four different particle systems are presented in this work, with the fibre type, sizing, base resin and particle volume fraction being consistent between the systems. The different material systems are described in Table 1. The (visible) particles in Materials B, C and D are made from the same thermoplastic, with Material A particles made from a different thermoplastic that features a notably different bridging behaviour. The invisible particles in Material C are suspected to have a similar density to the bulk resin (not distinguishable via CT) and a high interface strength (since they do not visibly de-bond). Although the composition of the materials is proprietary, the systems featured significantly different failure micro-mechanisms and initiation fracture toughness’s (G_{IC}’s), thus highlighting the importance of understanding their behaviour in order to develop more effective interlayers in the future.

System	Description	Particle V_f	Normalised $G_{IC\text{-}Pmax}$
Material A	5-10 µm spherical particles	13%	1.0
Material B	5-20 µm irregularly shaped particles	13%	0.80
Material C	Hybrid with 5-20 µm irregularly shaped and other particles invisible to CT	13%	0.64
Material D	20-40 µm irregularly shaped particles	13%	0.58

Table 1: Material systems overview

2.2 Fracture Toughness Testing

Standard 20 x 3 x 175 mm geometries with a 65 mm long PTFE insert were used for the Mode I fracture toughness tests, with five specimens tested for each material at a cross-head displacement rate of 2.5mm/min. Aluminium blocks were attached to the specimens, which were subsequently pre-cracked in Mode I, and reloaded to propagate the crack for 50mm in a double cantilever beam arrangement. A summary of the mean and standard deviation for the initiation fracture toughness calculated at peak load can be seen in Fig. 1. The initiation fracture toughness was calculated according to [16]:

$$\mathbf{G_I} = \frac{\mathbf{3P\delta}}{\mathbf{2Ba}} \tag{1}$$

where *P* is the load [N], δ is the cross-head displacement [m], *B* is the specimen width [m], and *a* is the crack length [m].

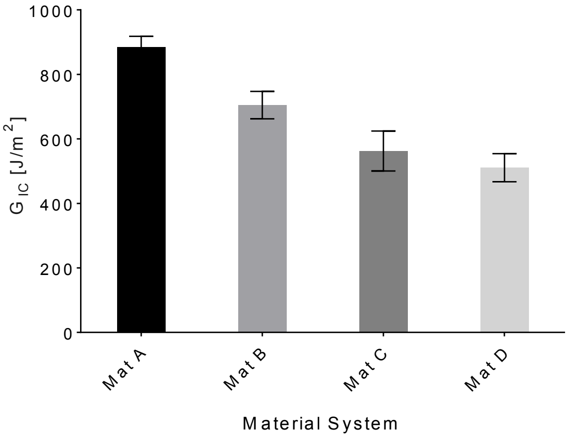

Figure 1: Mean and standard deviation for the Mode I initiation fracture toughness (G_{IC}) calculated at the peak load and corresponding displacement

2.2 Synchrotron Radiation Computed Tomography

SRCT was conducted at the Swiss Light Source (SLS) on the TOMCAT beamline at the Paul Scherrer Institut, Switzerland. Scans were conducted at a voxel resolution of 0.325 µm, with a detector size of 2560 x 2160 pixels. A beam energy of 15 kV was used, with 1501 projections taken at an exposure of 150 ms for the 180-degree rotation. A propagation distance of 23 mm was used to benefit from phase enhanced contrast, a technique that can improve the contrast of the edges between two materials of similar attenuation (explained in [17]). The 3D datasets were reconstructed at the SLS using the in-house GRIDREC method

[18]. Following acquisition, the Mode I cracks were segmented using Aviso Fire 8^{TM} and analysed in MATLAB^{TM}.

Following digital segmentation, the crack path was binarised and filtered to remove areas smaller than 5 pixels. Subsequently, the images were manually edited to leave only the main/'clean' crack profile. This was done for ten CT slices in the centre of the scanned volumes, spaced 100 slices apart. The filtered image was used for the COD analysis, with the 'cleaned' crack used for the ligament quantification following the method that is described in [12]. This process quantified the number of ligaments and summed the ligament thicknesses to determine the total interconnected area between the crack faces.

2.3 Specimen Geometry and Loading

A specimen cross-section of 2.5 x 3 mm was used in order to provide a uniform X-ray path through all angles of rotation. The small cross-section was chosen in order to maximise the transmission of low energy photons and ensure good scan contrast. The specimens were 150 mm long, with a 10 mm long PTFE insert placed at mid-plane to control the initiation of fracture. A wedge was driven into the mid-plane using a purpose built *in situ* rig seen in Fig. 2. The square ram ensured that no torsional loading was applied on the specimen during the experiment. An initial loading step grew the crack a distance of about 5 mm from the edge of the PTFE insert following which the specimen was scanned. The specimen was subsequently loaded to achieve about 200 μm of crack growth and scanned again, which was repeated three times. This allowed the crack growth to be captured in 3D in a time-resolved manner.

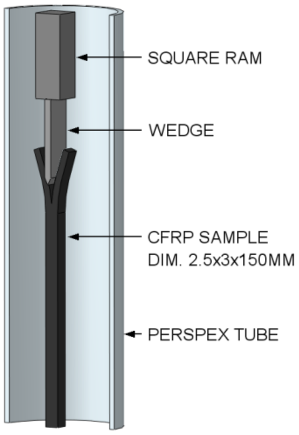

Figure 2: SRCT configuration for testing

3 COMPUTATIONAL MODELLING

3.1 Augmented Finite Element Method

AFEM is a numerical method that can treat arbitrary cracking problems that can initiate and propagate cracks according to a predefined cohesive law. The ability for the elements to host multiple cracks makes the method suitable for studying the damage evolution observed in the systems presented in this work. The elements can be integrated into standard Finite Element (FE) packages, such as ABAQUS^{TM} via user subroutines, because the method uses standard finite element shape functions. AFEM was developed by Ling et al. [15] and is based on using elements with double nodes (physical and ghost). If an element is not cut by a crack, then the Degrees of Freedom (DoFs) of the ghost nodes are equated to those of the physical nodes, reducing the problem to standard FE shape function. However, if the element is severed by a crack, the two physically separate physical domains can be approximated using two Mathematical Elements (MEs) containing both physical and ghost nodes. The stiffness and force integration can then be calculated over the active domain within each ME separately, following which a cohesive failure description across the crack line connects the two MEs together. The method allows for different displacement fields in the two physical domains that permit it to account for discontinuous displacements (or displacement jumps) across the cohesive crack. More information can be found in Ling et al. [15]

3.2 Preliminary Numerical Model

Figure 3 illustrates the interlayer between the two plies with three embedded 'strong discontinuities'/de-bonds (i.e. no traction across the faces) placed in the region of interest after an initial pre-crack. The dotted line along the bottom of the interlayer indicates the placement of a 'weak' discontinuity, such that the elements will only crack along the interface should the peak cohesive stress be exceeded. The model is pinned on the right hand side, and a displacement controlled loading is applied on the top and bottom plies on the left hand side. Two separate element definitions were given to the neat resin and the ply/interface elements, such that the effects of the relative toughness's between the two competing mechanisms could be explored with respect to the crack path. The thickness of the interlayer is consistent with the ~ 30 μm dimensions seen in the CT data, and stiffness of the resin was taken to be 4GPa, with the neighbouring ply stiffness of 300GPa. Currently, there is limited information regarding suitable cohesive parameters to define resin and ply interface properties at such length-scales, so only the relative toughness's between the two competing mechanisms was explored in this work. This was done by changing the critical cohesive stress whilst maintaining the shape parameter and critical opening. At this time, the Mode I and Mode II cohesive strengths were assumed to be equal in this preliminary work.

The output of the model determines how many discontinuities are followed as the proportion of de-bonds/'strong discontinuities' ahead of the tip is reduced. In doing so, the effects of the neighbouring ply stiffness (between 150 – 3000 GPa), and the relative toughness's between the ply/interface and resin (between 0.6 – 0.8) on the crack path could be explored. Fig. 4 (a) - (d) illustrate the four potential outcomes that are supported by the model, whereby the crack path can follow from zero to three discontinuities in the region of interest. Fig. 4 (e) shows an example of the crack path reaching the region of interest, following which the ply/interface fails and draws the crack path towards it with complete separation shown in Fig. 4 (f). The extent of the fraction of discontinuities is intended to simulate potential particle de-bond locations as the particle volume fraction is decreased, and/or an increasing particle interface strength.

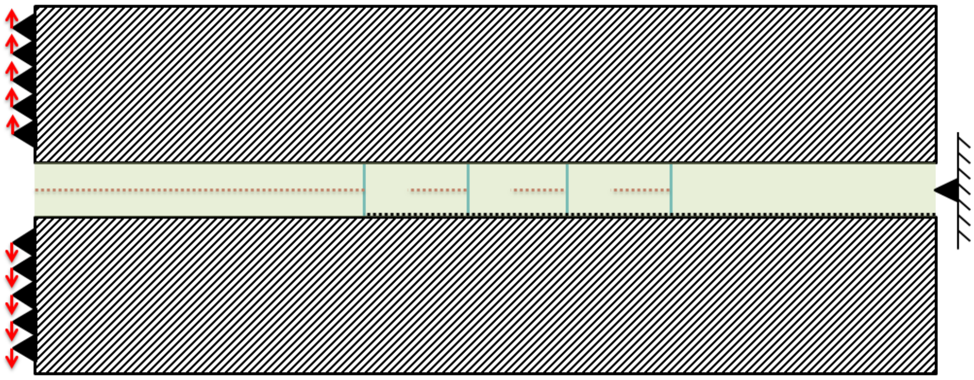

Figure 3: Illustration of the interlayer models and the region of interest containing ‘strong discontinuities’/ de-bonds in each subset (not to scale)

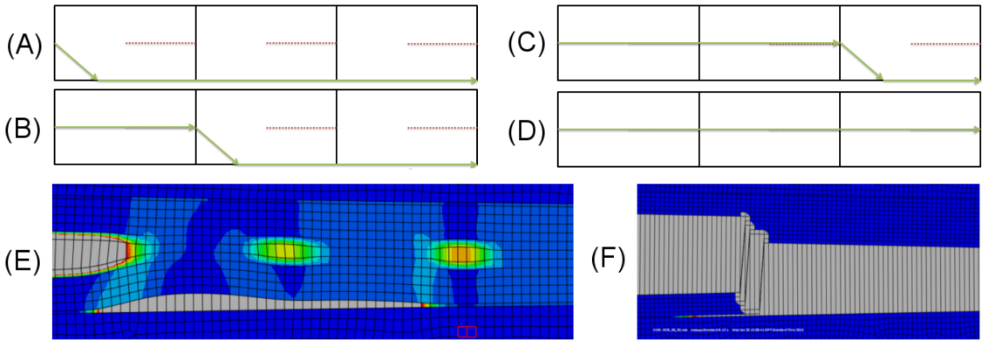

Figure 4: Illustration of the potential model outputs (a-d) and example model results (e-f)

RESULTS

The damage evolution captured during the multiple load steps conducted in this work captured a total crack growth of about 1 mm. Figures 4 and 6 illustrate a ~200 µm crack growth step that was chosen to illustrate the level of detail that can now be captured using these time-resolved experiments. The crack growth direction is from left to right, with the post-growth slice placed below the corresponding pre-growth image. The quantitative analysis was conducted on two rastered scans that were stitched together to capture about 1.0 mm of the Mode I crack wake.

4.1 Mode I Damage Evolution

Fig. 5(a) shows the Mode I 'crack tip' in Mat. A, where the damage progression was identified to initiate from particles cracking from within, followed by crack coalescence, and the formation of particle-bridging ligaments. Particles only appear to partially de-bond closer to the developing 'main crack', indicating that the particle/resin interface is relatively strong. This suggests that the bridging mechanism (in this material) originates from the ability for the particles to plastically deform whilst remaining bonded to the crack flanks. However, the bridging ligaments in Mat. B are formed from the surrounding epoxy resin rather than the particles. This is seen in Fig. 5(b), which clearly shows that the particles in this system de-bond too readily to be effective at providing toughness enhancing traction forces. In the 3D volume, larger ligaments are seen to occur that are formed from a combination of particle and resin, but predominantly smaller resin-only ligaments are featured in this material system. Fig 5 also highlights the microstructural irregularity seen in these systems, with stray fibres in the interlayer (Fig. 5(a)), particle depleted regions (Fig. 5(b)), and a range of particle sizes. Previous work has shown that the crack path preferentially follows particle de-bonds, and that large particle-depleted regions will result in the crack propagating towards the ply/interface [13], so understanding the effects of the microstructure is critical.

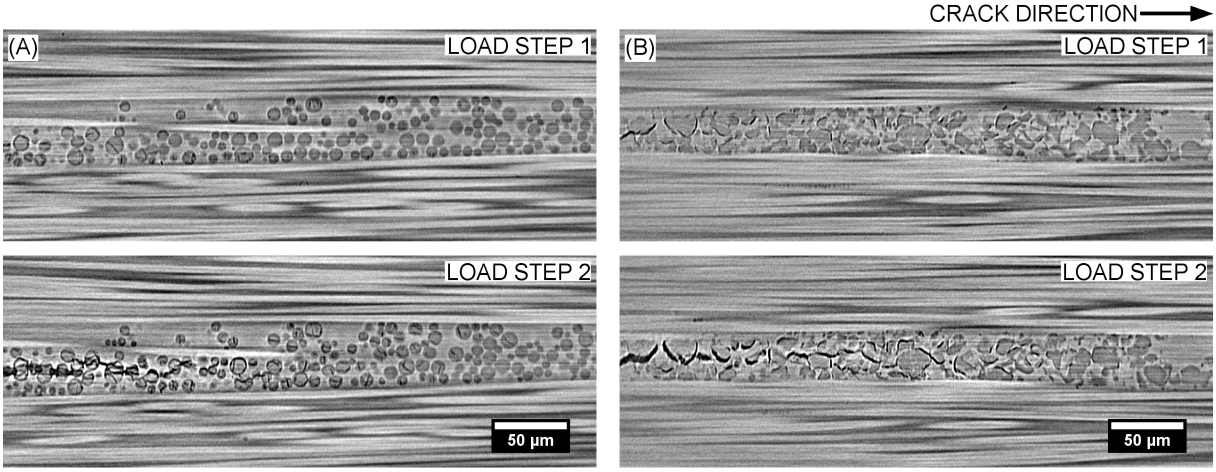

Figure 5: Mode I damage evolution following a load step in (a) Mat. A and (b) Mat. B

Fig. 6(a) shows the crack progression in Mat. C, where the microstructure appears highly divided between the top and the bottom of the interlayer. The visible particles (same as Mat. B) are dispersed over the top of the interlayer and have de-bonded as seen previously in Fig. 5(b). The particles along the bottom were not observed to de-bond, suggesting that the effective interface strength between these particles and the surrounding resin is stronger than the visible particles. This relative strength is one that could be explored through modelling. The crack path follows these de-bonded particles, with the bridging ligaments formed from the bulk resin. About 50 μm from the left hand side of Fig. 6(a), there is clear indication of a failing ligament. The remaining ligament has visibly thinned providing evidence that the epoxy does deform plastically, which supports previous authors' findings of plastic deformation [19]. Examining the whole volume, intralaminar failure is observed to occur in about 12% of the scanned volume, which was not observed for the other materials. This may imply that the lack of readily de-bonding particles ahead of the tip has caused the crack path to enter a more energetically favourable region. Fig. 6(b) shows the crack path in Mat. D. The variation of particle size in this microstructure is more evident, and qualitatively, it appears that larger particles de-bond more readily than the smaller ones. As with Mat. B and C, the bridging ligaments in this system are formed from the epoxy resin. Smaller resin strands are present along with thicker ligaments (seen at the left hand side of the image). A small sharp crack appears on the right hand side of this particular ligament, suggesting that this larger ligament is likely to fracture before it can be deform to the same extent as the smaller resin strands.

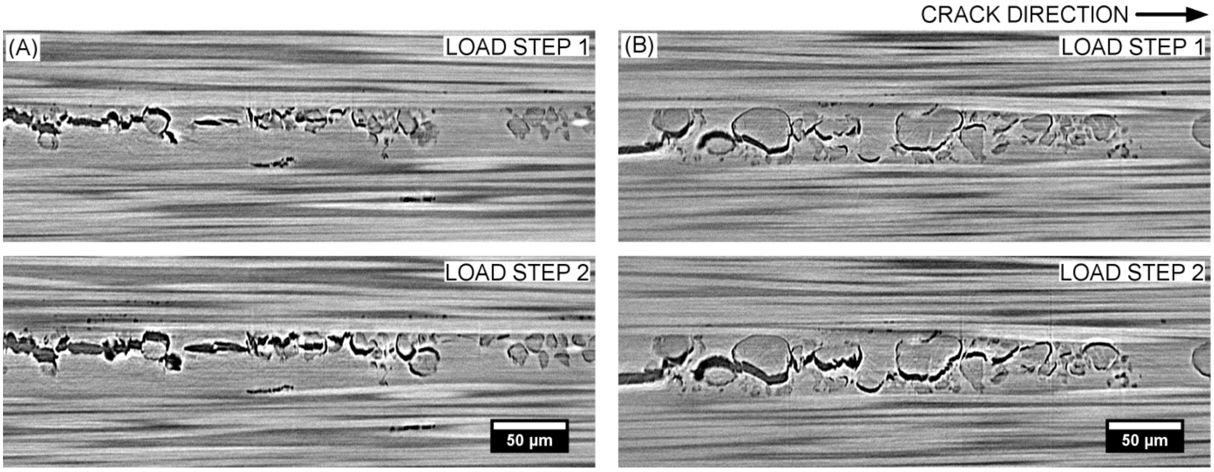

Figure 6: Mode I damage evolution following a load step in (a) Mat. C and (b) Mat. D

4.2 Crack Path Quantification

Fig. 7(a) shows the CODs for all the material system. It must be acknowledged that the data for Mat. C may not be representative since the wake of the crack was not captured to the same extent as the other materials. However, it is clear that for Mat. A, that there is a significant dip in the COD curve, which are an indicator for traction forces. On either side of this dip, there is a noticeable change in gradient, with the steeper gradient in the wake indicative of poorer traction forces since the rate of opening is higher. This feature is also present, but to a lesser extent in Mat. D. These changes in gradient could be used to estimate the critical opening of a cohesive zone law, and may suggest that a value of about 0.6 mm may be a suitable. This would be comparable to the previously reported critical opening values of about 0.5 mm [20]. Mat. B, C and D have a similar final slope to each other, which differ to the larger gradient found in Mat. A, and may suggest that the type of bridging ligaments are having an effect, whereby Mat. A ligaments consist of thermoplastic particles rather than epoxy resin.

Fig. 7(b) and (c) show the average interconnectivity and average number of ligaments for the material systems respectively. It appears as though the number of ligaments relates to the G_{IC} of the material systems seen in Table 1, while the average interconnectivity does not correlate to the toughness rankings. Looking at the Mat. B and D (whose thermoplastic particles are of the same material), the smaller particles promote a higher number of ligaments forming. Geometrically this makes sense, since for the same particle volume fraction there are more opportunities for ligaments to form between the larger numbers of particles. The larger interconnectivity, seen with the larger particles (Mat. D), may be capturing particles that separate two cracks, but these bridges are not effective because the particles have been observed to readily de-bond. The larger sized resin ligaments seen in Fig. 6(b) may also be less effective, since a larger ligament may fracture prior to being able to provide significant traction. Therefore, it is suspected that the deformation of the smaller resin ligaments is more critical than the overall interconnectivity.

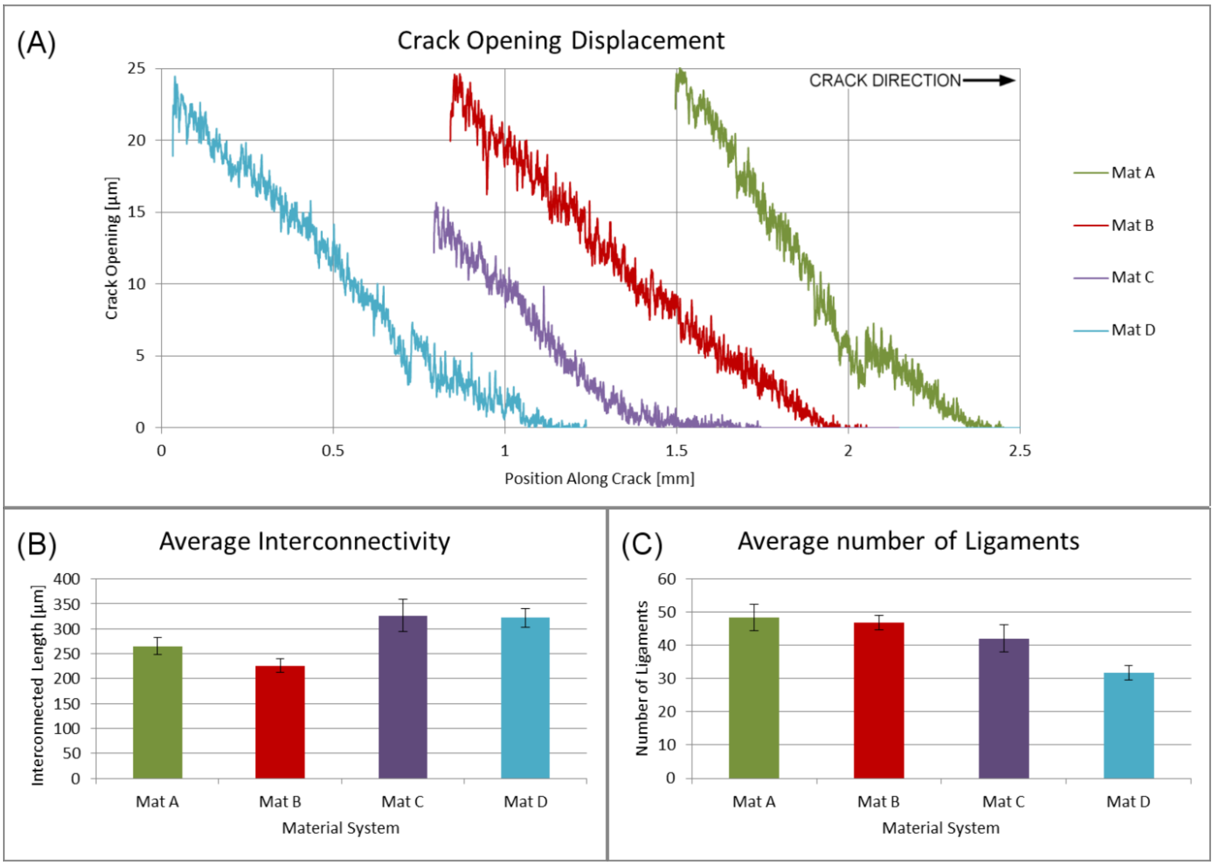

Figure 7: Showing the mean and mean deviation for: (a) crack opening displacement, (b) interconnectivity, and (c) number of ligaments quantified for the different material systems

4.4 Crack Path Modelling

From the CT data, it is apparent that the presence of de-bonds ahead of the main crack are key to keeping the crack away from the ply/interface, since particle-depleted regions have been seen to promote crack propagation along the ply interface. Fig. 8(a) shows the effects of varying the relative cohesive strength between the resin and the ply/interface. The extent of de-bonding ahead of the crack tip was explored by varying the fraction of discontinuities in the subsets shown in Fig. 4. It was shown that as this fraction reduced, that the crack path was drawn towards the ply sooner. This may simulate the effect of particle-depleted regions and/or a toughened interlayer with a lower particle volume fraction. Fig. 8(b) shows that varying the ply stiffness from 150GPa – 3000GPa has no significant effect on the crack path. However, it is clear in Fig. 8(a) that the relative strength/toughness of the ply/interface is critical to the crack path, where a low ply/interface strength will provide the lower energy crack path and result in crack propagation along the interface sooner. Although this is currently quite an abstract representation of the real systems, the 'strong'/traction free discontinuities can be given properties allowing the simulation of the competition between the particle interface, ply interface and neat resin properties to be explored.

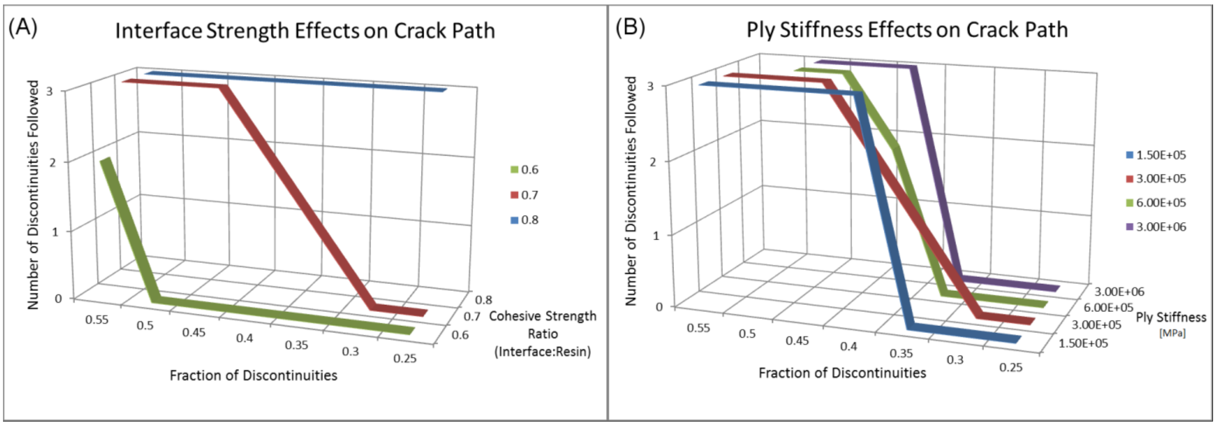

Figure 8: Illustration showing (a) significant effects of the relative resin to ply/interface toughness's and (b) no real effect being caused by the ply

5 CONCLUSIONS AND FURTHER WORK

The results presented in this work are targeted at increasing the understanding surrounding key mechanisms contributing to the toughness of interlayer-toughened systems. To the best of the authors' knowledge, these time-series experiments are the first to capture Mode I crack growth in these material systems at such high resolutions, thus removing any doubt surrounding whether particles are reacting to the applied loads, or whether they were previously cracked/de-bonded. Quantification of the crack paths has suggested the larger particles in Mat. D promoted the formation of a fewer number of large bridging ligaments, which resulted in a lower G_{IC} when compared to the smaller particles of Mat. B. Although the extent of interconnectivity was higher for the larger particles, the results suggest that a larger number of small ligaments can be correlated to a higher G_{IC}. Mat. A, with the highest G_{IC}, had the most significant change in its COD following a notable dip in the curve, which indicated that there is a highly effective traction mechanism occurring in the first 0.6 mm of crack length. The bridging ligaments in this material were formed from the thermoplastic particles themselves, rather than of the epoxy resin seen for the other material systems.

The preliminary model has shown that the competition between the resin and ply interface properties is important in determining the crack path, along with the extent of discontinuities ahead of the main crack front. It is thought that the optimum microstructure will feature just the right amount of de-bonds in order to keep the crack away from the ply interface. Future work will aim to give the current 'strong discontinuities' cohesive properties to simulate the particle bridging seen in Mat. A, and eventually build towards using particles with interfaces to build a more physically representative model.

ACKNOWLEDGEMENTS

The authors acknowledge contributions from institutions and staff: Cytec Engineered Materials Ltd. for their sponsorship and materials supply, and the support from Dr. Kingsley Ho as the technical point of contact. The μ-VIS centre at the University of Southampton for provision of tomographic imaging facilities, supported by EPSRC grant EP-H01506X, and the support from Dr. Richard Boardman and Dr. Neil O'Brien. The support from researchers Derek Schesser and Bao-Chan Do from the Univeristy of Miami. Additionally, the authors acknowledge support from Dr. Peter Modregger at the Swiss Light Source and funding from the Community's Seventh Framework Programme (FP7/2007-2013) under grant agreement n.°312284 (for CALIPSO).

REFERENCES

[1] M. O. W. Richardson and M. J. Wisheart, "Review of low-velocity impact properties of composite materials," *Compos. Part A*, vol. 27, pp. 1123–1131, 1996.
[2] M. Yasaee, I. P. Bond, R. S. Trask, and E. S. Greenhalgh, "Mode I interfacial toughening through discontinuous interleaves for damage suppression and control," *Compos. Part A Appl. Sci. Manuf.*, vol. 43, no. 1, pp. 198–207, Jan. 2012.
[3] M. Yasaee, I. P. Bond, R. S. Trask, and E. S. Greenhalgh, "Mode II interfacial toughening through discontinuous interleaves for damage suppression and control," *Compos. Part A Appl. Sci. Manuf.*, vol. 43, no. 1, pp. 121–128, Jan. 2012.
[4] S. Singh and I. K. Partridge, "Mixed-Mode Fracture in an Interleaved Carbon-Fibre/Epoxy Composite," *Compos. Sci. Technol.*, vol. 55, pp. 319–327, 1996.
[5] S.-Y. Fu, X.-Q. Feng, B. Lauke, and Y.-W. Mai, "Effects of particle size, particle/matrix interface adhesion and particle loading on mechanical properties of particulate–polymer composites," *Compos. Part B Eng.*, vol. 39, no. 6, pp. 933–961, Sep. 2008.
[6] M. Zamanian, M. Mortezaei, B. Salehnia, and J. E. Jam, "Fracture toughness of epoxy polymer modified with nanosilica particles: Particle size effect," *Eng. Fract. Mech.*, vol. 97, pp. 193–206, Jan. 2013.
[7] A. G. Evans, Z. B. Ahmad, D. G. Gilbert, and P. W. R. Beaumont, "Mechanisms of toughening in rubber toughened polymers," *Acta Met.*, vol. 34, no. 1, pp. 79–87, 1986.
[8] Y. Huang and A. J. Kinloch, "Modelling of the toughening mechanisms in rubber-modified epoxy polymers A quantitative description of the microstructure-fracture I ~," *J. Mater. Sci.*, vol. 27, pp. 2763–2769, 1992.
[9] Y. Huang and A. J. Kinloch, "The sequence of initiation of the toughening micromechanisms in rubber-modified epoxy polymers," *Polymers (Basel).*, vol. 33, no. 24, pp. 5338–5340, 1992.
[10] M. R. Groleau, Y. Shi, A. F. Yee, J. L. Bertram, H. J. Sueb, and P. C. Yang, "Mode II Fracture of Composites Interlayered with Nylon Particles," *Compos. Sci. Technol.*, vol. 56, pp. 1223–1240, 1996.

[11] N. Sela and O. Ishai, “Interlaminar fracture toughness and toughening of laminated composite materials: a review.,” *Composites*, vol. 20, no. 5, pp. 423–35, 1989.
[12] D. J. Bull, A. E. Scott, S. M. Spearing, and I. Sinclair, “The influence of toughening-particles in CFRPs on low velocity impact damage resistance performance,” *Compos. Part A Appl. Sci. Manuf.*, vol. 58, pp. 47–55, Mar. 2014.
[13] G. Borstnar, M. N. Mavrogordato, L. Helfen, I. Sinclair, and S. M. Spearing, “Interlaminar fracture micro-mechanisms in toughened carbon fibre reinforced plastics investigated via synchrotron radiation computed tomography and laminography,” *Compos. Part A Appl. Sci. Manuf.*, vol. 71, pp. 176–183, Apr. 2015.
[14] H.-M. Hsiao, C.-N. Ni, M.-D. Wu, and C.-W. Lin, “A novel optical technique for observation of global particle distribution in toughened composites,” *Compos. Part A Appl. Sci. Manuf.*, vol. 43, no. 9, pp. 1523–1529, Sep. 2012.
[15] D. Ling, Q. Yang, and B. Cox, “An augmented finite element method for modeling arbitrary discontinuities in composite materials,” *Int. J. Fract.*, vol. 156, no. 1, pp. 53–73, May 2009.
[16] S. Hashemi, A. J.- Kinloch, and J. G. Williams, “Mechanics and Mechanisms of Delamination in a Poly (ether sulphone) - Fibre Composite,” *Compos. Sci. Technol.*, vol. 37, pp. 429–462, 1990.
[17] P. Cloetens, M. Pateyron-Salomé, J. Y. Buffière, G. Peix, J. Baruchel, F. Peyrin, and M. Schlenker, “Observation of microstructure and damage in materials by phase sensitive radiography and tomography,” *J. Appl. Phys.*, vol. 81, no. 9, p. 5878, 1997.
[18] F. Marone and M. Stampanoni, “GRIDREC software,” *J. Synchrotron Rad.*, vol. 19, pp. 1029–1037, 2012.
[19] R. Bagheri, B. T. Marouf, and R. a. Pearson, “Rubber-Toughened Epoxies: A Critical Review,” *Polym. Rev.*, vol. 49, no. 3, pp. 201–225, Aug. 2009.
[20] Q. Yang and B. Cox, “Cohesive models for damage evolution in laminated composites,” *Int. J. Fract.*, vol. 133, no. 2, pp. 107–137, May 2005.